Triplet-pair spin signatures from macroscopically aligned heteroacenes in an oriented single crystal

Brandon K. Rugg[a], Kori E. Smyser[b], Brian Fluegel[a], Christopher H. Chang[a,c], Karl J. Thorley[d], Sean Parkin[e], John E. Anthony[d,e], Joel D. Eaves[b,c], and Justin C. Johnson[a,c,1]

The photo-driven process of singlet fission generates coupled triplet pairs (TT) with fundamentally intriguing and potentially useful properties. The quintet $^5TT_0$ sublevel is particularly interesting for quantum information because it is highly entangled, is addressable with microwave pulses, and could be detected using optical techniques. Previous theoretical work on a model Hamiltonian and nonadiabatic transition theory, called the *JDE* model, has determined that this sublevel can be selectively populated if certain conditions are met. Among the most challenging, the molecules within the dimer undergoing singlet fission must have their principal magnetic axes parallel to one another and to an applied Zeeman field. Here, we present time-resolved electron paramagnetic resonance (TR-EPR) spectroscopy of a single crystal sample of a tetracene-thiophene compound featuring arrays of dimers aligned in this manner, which were mounted so that the orientation of the field relative to the molecular axes could be controlled. The observed spin sublevel populations in the paired TT and unpaired (T+T) triplets are consistent with predictions from the *JDE* model, including preferential $^5TT_0$ formation at $z \parallel B_0$, with one caveat—two ^5TT spin sublevels have little to no population. This may be due to crossings between the ^5TT and ^3TT manifolds in the field range investigated by TR-EPR, consistent with the intertriplet exchange energy determined by monitoring photoluminescence at varying magnetic fields.

magnetic resonance | quantum information | singlet fission | triplet pair | photophysics

Technologies that utilize quantum information (QI) have the potential to transform the fields of computation, sensing, and communications. Still, such applications are currently beyond reach, in large part because of difficulties that prevent sufficient scaling of conventional material architectures currently used to store registers of qubits, or units of QI (1, 2). However, the bottom-up approach of designing, synthesizing, and optimizing molecules to serve as spin qubit candidates has emerged as a promising alternative, as molecular qubits can achieve long coherence times, are amenable to organization in extended qubit structures in a controlled fashion, and enable photophysical control (3, 4).

Among molecular candidates, singlet fission (SF) materials are worthy of attention, as they can form pure, entangled quantum states involving two triplet excitons (T) upon photoexcitation, even at room temperature (5–8). In addition to the possibility of selective state population, the two-exciton states resulting from SF have already shown near-microsecond coherence times well above milliKelvin temperatures required for other systems, enabling spin manipulation and characterization via pulsed electron paramagnetic resonance (EPR) experiments (9–11). As an example, it has been demonstrated that the polarization of the exciton pair TT can be transferred to specific nuclei on the same molecule using controlled microwave pulses (9), which may allow for a hybrid qubit that takes advantage of the higher polarization, faster manipulability of electron spins, and the much longer coherence times of nuclear spins (12). Furthermore, optical readout of the spin state is inherent to many molecular qubits (13–15).

The spin-conserving evolution of an excited singlet exciton ($S_1 + S_0$) on a chromophore pair to the overall singlet ^1TT, delocalized over both chromophores, is the first step of SF (16). In addition to the ^1TT state, there are three triplet ^3TT and five quintet ^5TT sublevels, split from ^1TT by J and $3J$, respectively, where J is the intertriplet exchange interaction (Fig. 1A). The relative ordering of the spin state manifolds is dictated by the sign of J, with a negative, or ferromagnetic J indicating that the ^5TT state is lowest in energy. While J has a large impact on the evolution of TT sublevel populations (17), the splitting of transitions observed in EPR experiments is primarily affected by the spin dipole–dipole interaction between the two electron spins within a single triplet species (T) (Fig. 1B).

Significance

Producing ordered elements of quantum information, such as aligned electron spins in an ensemble of atoms, is challenging at large scales and practical temperatures. Toward this end, we have modelled and characterized crystals of a tailored molecule that aligns with macroscopic order and possesses photo-initialized species with characteristic and well-resolved spin signatures in magnetic resonance experiments that measure key spin–spin interactions for molecular pairs. Rotating the crystal with respect to the magnetic field produces populations of specific spin states that are macroscopically and deterministically controlled at room temperature. Explained through rigorous theoretical modeling, the pure spin polarization and its dependence on orientation advance molecular approaches to relevant length- and timescales for quantum sensing and computation.
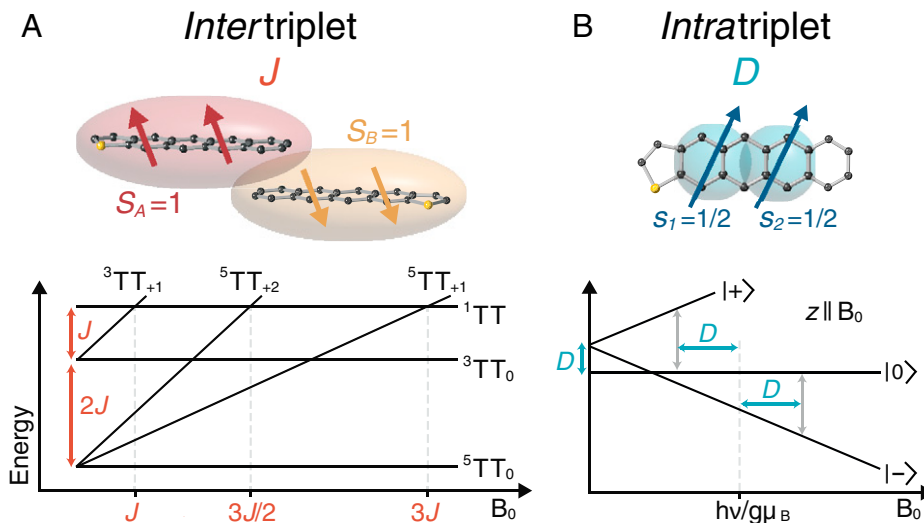
Fig. 1. Schematic and associated energy level diagrams for (A) the intertriplet interaction J, which dictates energetic splitting between the ^1TT, ^3TT, and ^5TT spin manifolds (depicted for negative J in the diagram) and is dependent on the degree of electronic coupling between triplet excitons. The magnitude of J can be obtained directly by measuring field strengths at which PL is decreased due to mixing of the emissive ^1TT state with dark ^5TT sublevels. (B) The intratriplet interaction D, which primarily dictates energetic splitting between magnetic sublevels within T+T, ^3TT, and ^5TT. Splitting of TR-EPR transitions due to D is dependent on molecular orientation relative to an applied magnetic field (B_0); the energy level diagram depicts the splitting between the states of an isolated T when the primary molecular axis (z) is parallel to B_0, for which associated transitions are split by $2D$. Values of D and its associated parameter E (not depicted) are typically obtained from fitting the TR-EPR powder spectrum of triplets localized on noninteracting monomers.

Smyser and Eaves (6) previously developed a model, based on nonadiabatic transition theory (NTT), for dimers whose molecules share principal axis directions. In this *JDE* model, named for the parameters in the hamiltonian, the effective J is large enough to separate the ^{2S+1}TT states, but immediately following SF, large fluctuations in J induce crossings between the various $^{2S+1}TT_M$ sublevels to facilitate relaxation events (18). The subsequent sublevel population is dictated by the orientation of the molecular z axis relative to an applied magnetic field (B_0). Importantly, for QI applications, the $^5TT_0$ sublevel is dominant for $z \parallel B_0$, and there is evidence that it is addressable with microwave pulses and has the potential for optical readout (15, 19, 20). In this paper, we expand the model to include exciton unbinding dynamics that can occur in crystals with mobile excitons and find that the separated triplets (T+T) maintain the spin polarization of the initially formed sublevels.

Motivated by the predictions of the *JDE* model, we have conducted a time-resolved EPR (TR-EPR) study of a single crystal of 2-triethylsilyl-5,11-bis(triisopropylsilyl ethynyl) tetraceno[2,3-b]thiophene (TES TIPS-TT), a heteroacene with a crystal structure in which all molecules share a common z axis (Fig. 2). The macroscopic properties of the TES TIPS-TT crystal also permit samples to be prepared so that the angle (θ) of the molecular z axis relative to B_0 can be systematically controlled. This approach allows for an unprecedented look into the orientation dependence of spin evolution relative to previous studies of ^5TT, which have employed disordered samples or have at best achieved partial ordering (10, 21–23). Other single crystal studies of SF materials, such as one performed on tetracene, did not directly observe TR-EPR signal from ^5TT (24), although one recent study did report orientation-dependent TR-EPR spectra, including ^5TT features with
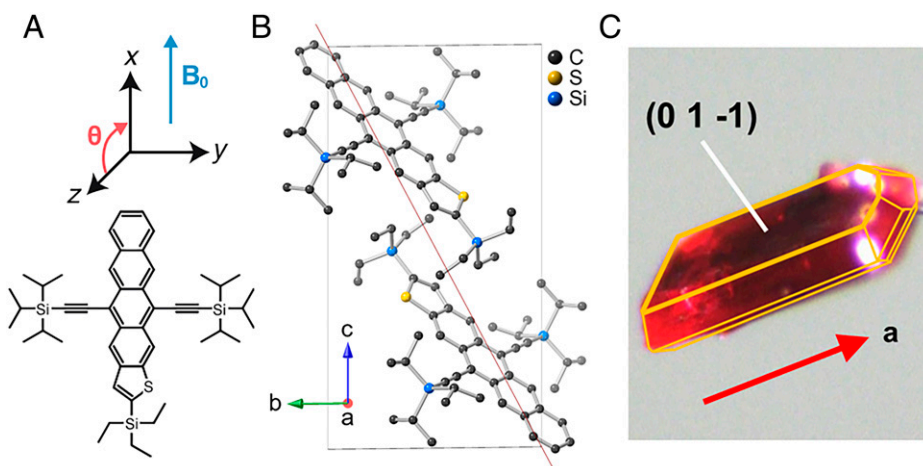

Fig. 2. TES TIPS-TT molecular and crystal structure. (A) Molecular coordinate system. The primary axis z is perpendicular to the molecular π-system, and its orientation relative to B_0 is defined by θ. The illustration shows $\theta = 90°$, or $x \parallel B_0$. (B) Crystal structure of TES TIPS-TT from the view along the a axis, with the (0 1 -1) face indicated by a red line. The S atoms in both molecules appear on either side of the thiophene ring with equal likelihood. H atoms are hidden. (C) Photograph of a representative TES TIPS-TT crystal, which typically forms a tablet-shaped monolith with its major face aligned with the (0 1 -1) plane and its long axis equivalent to the a axis of the crystal structure.

microsecond-scale coherence times (11). The principal molecular axes of the molecules in the unit cell of the tetracene derivative used in that study are not parallel, and the absolute crystal orientation was not identified in TR-EPR spectra nor were sublevel populations compared against a rigorous model. For TES TIPS-TT studies described here, sublevel populations of photoexcited triplet pairs are well-described by the *JDE* model at all specified orientations of the indexed crystal. However, primarily absorptive or anomalously broadened TR-EPR features are also observed that require a more detailed understanding of dynamics in this crystalline material. Nonetheless, routes toward a selective population of $^5TT_0$ are outlined, laying the groundwork for further studies of the quantum properties of this state.

Results

Structural Characterization. Knowledge of the microscopic and macroscopic crystal properties of TES TIPS-TT enables a high level of control over molecular orientation relative to B_0 in TR-EPR experiments. The unit cell features two unique inversion-related molecules of TES TIPS-TT that are defined by a common molecular z axis, which simplifies both the spin dynamics of the SF exciton pair and interpretation of the associated TR-EPR spectra relative to an unaligned chromophore pair (6). We note that prior work on a series of related tetraceno-bithiophene derivatives discovered high mobility in thin-film transistors and related this behavior to the slip-stacked packing found in single crystals, suggesting strong and extended π–π interactions (25). Here, the substitution of an alkylsilyl group on the thiophene ring enforces asymmetry that renders primarily distinct dimer types into the structure. In addition to the dimer observable in the unit cell that has the thiophene rings partially eclipsed (Fig. 2*B*), each chromophore is also similarly coupled to another neighboring molecule, but with the thiophenes on opposite sides and the terminal phenyls partially eclipsed (Fig. 3, dimer II). This series of stacked dimers continues in a staircase-like fashion. Perpendicular to this direction, there are two varieties of "side-by-side" dimers, which appear to be much more weakly coupled (Fig. 3, dimer III). While not likely to be the dominant sites for SF, due to the lack of strong orbital overlap, these nearly coplanar dimers may play a role in supporting weakly coupled triplet pairs upon diffusion and nongeminate encounters.
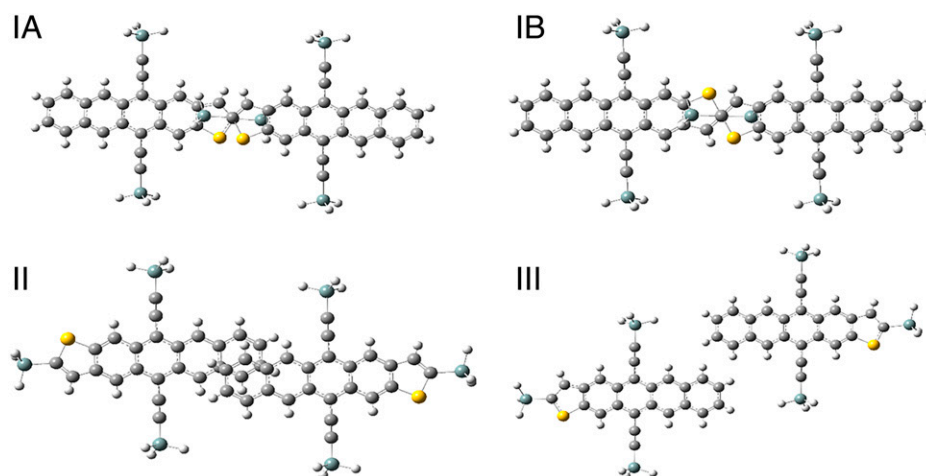
Table 1. DFT-calculated exchange couplings for TES TIPS-TT dimers

Dimer model	Calculated exchange coupling (GHz)
IA	−15
IB	35
II	−315
III	<1

TES TIPS-TT forms tablet-shaped crystals with a clearly identifiable long axis and a parallel set of two large faces (Fig. 2*C*). The results obtained from indexing several crystals indicate that the long axis corresponds to the crystallographic *a* axis, and the large faces correspond to the (0 1 -1) and (0 -1 1) planes of the unit cell. Combining this information with the orientation of the molecules within the unit cell, it is determined that the molecular z axes of all chromophores within a single-crystal sample could be aligned with B_0 by mounting the crystal to quartz rods cut at 38°, as shown in *SI Appendix*, Fig. S6. Rotation of the EPR sample rod permits careful control of the orientation of both the x and z axes relative to B_0, while the y axis remains perpendicular.

Calculations. Table 1 shows calculated exchange couplings for four dimer models with optimized geometries (Fig. 3) from density functional theory (DFT) methodology benchmarked with a zero-field splitting (ZFS) calculation testing various functionals (details can be found in *SI Appendix*) Dimers IA and IB are nearly identical and only differ in whether sulfur positions were modeled on the same or opposite sides, respectively, of a plane encompassing the long molecular axes of the dimer pair.

Dimers IA and IB have similar exchange coupling magnitudes but of opposite signs. When the sulfur atoms are on opposite sides of the aromatic core (IB), the quintet state is higher in energy than the singlet state (i.e., antiferromagnetic coupling). Dimer model IA shows a ferromagnetic coupling of comparable magnitude to that observed experimentally (vide infra). The primary interaction for these dimers is through the thiophene rings. In contrast, dimer II involves the interaction between the distal tetracene ends. Both enhanced spatial overlap and intermolecular proximity may explain the larger calculated exchange coupling for dimer II, as the molecular planes

Fig. 3. Dimer pairs for which exchange couplings were calculated. Dimers IA and IB differ in the modeled disorder of sulfur atoms in the crystal structure. Images have phenyl rings in the plane of the page.

are separated by 3.3 Å, compared to 5.1 Å for IA/B. Dimer III involves side-by-side molecules and possesses minimal exchange splitting between the broken-symmetry singlet and quintet states (the raw energy difference was calculated to be -0.018 GHz). Previously published calculations for crystalline TIPS-tetracene also show large variations in J ranging from ≈ 60 GHz to <1 GHz for nearest-neighbor pairs that have significant vs. minimal cofacial overlap (26). The methodology used here differs in the choice to include peripheral Si atoms and to employ a broken symmetry vs. explicitly multireference approach.

Magnetophotoluminescence. Single crystals of TES TIPS-TT exhibit several bands of steady-state fluorescence in the range of 600 to 800 nm when excited at 519 nm (*SI Appendix*, Fig. S7). The yield of the fluorescence within the range of 700 to 775 nm shows a clear dependence on the strength of an applied magnetic field at low temperatures (Fig. 4A). Dips in the fluorescence intensity are observed where the nonmagnetic ^1TT state crosses with the dark ^5TT_M sublevels that tune through the magnetic Zeeman interaction (19). The magnitude (though not sign) of J can be determined from the distribution of the dips in the spectrum. The experimental field range (0 to 14 T) allows for the detection of J between roughly 5 and 131 GHz. As it appears to be most consistent with the DFT calculations

and TR-EPR spectra (vide infra), we assume ferromagnetic coupling, as shown in Fig. 4B.

Two prominent dips in the field sweep appear at 0.83 and 1.65 T. Based on the 1:2 ratio of these values, and assuming $J < 0$, the first and second peaks can be assigned to ^1TT mixing with $^5TT_{+2}$ and $^5TT_{+1}$ (Fig. 4B). This occurs at field strengths of about $1.5|J|$ and $3|J|$, respectively, so that $|J| = 15.4 \pm 0.3$ GHz for at least one dimer within the TES TIPS-TT crystal structure. No dip is detected at the $^1TT - {}^3TT_{+1}$ curve crossing field position (at $|J|$, dashed line in Fig. 4). Its absence here is not related to excessive broadening, as a peak at J should have the same width as the feature at $3J/2$ (20). A dip and subsequent rise are observed at low field, but no other features are found up to 14 T (*SI Appendix*, Fig. S8).

These results are similar to those previously obtained from TIPS tetracene (19), which we have reproduced using a single crystal sample to verify the instrument sensitivity (*SI Appendix*, Fig. S9). However, three peaks (rather than just two) were observed for TIPS tetracene. In addition to the peaks consistent with $^5TT_{\pm2}$, and $^5TT_{\pm1}$ mixing with ^1TT, there is also a peak at J, suggesting mixing with $^3TT_{\pm1}$. This yields a characteristic 1:3/2:3 splitting pattern that was observed by Bayliss et al. (19) for multiple dimer sites within semicrystalline samples of TIPS tetracene.

EPR Spectroscopy. TR-EPR spectra of TES TIPS-TT in a 4:1 mixture of iodobutane and toluene after $\lambda_{ex} = 600$ nm were collected at 100 K (*SI Appendix*, Fig. S10). The heavy atom effect from the solvent encourages intersystem crossing (ISC) in the solute, allowing the triplet state of isolated TES TIPS-TT molecules to be characterized. Fitting the extracted spectrum indicated ZFS parameters of $D = 1{,}273$ MHz and $E = -40$ MHz. These parameters represent the axial (z) and transversal (x, y) components of the spin dipole–dipole interaction of T represented in Fig. 1B. They also inform on the field range for the ^3TT, ^5TT, and T+T spectral features in EPR from crystalline TES TIPS-TT. The two prominent peaks observed in the triplet powder spectrum (e.g., around 325 and 370 mT) are associated with the statistically favored $z \perp B_0$ orientation and are split by $|D - 3E|$.

TR-EPR spectra obtained from a crystalline powder of TES TIPS-TT at room temperature after $\lambda_{ex} = 610$ nm are shown below the crystal spectra in Fig. 5 and are expanded in *SI Appendix*, Fig. S10 for comparison with the solvated molecule spectra. Qualitatively, the presence of $^5TT_0$ in the early time 25- to 75-ns spectrum can be inferred from the presence of a pair of peaks, namely, one emissive and one absorptive, split from each other about center field by approximately $|D|/3$ (10, 22). Other features in the spectrum, that are primarily absorptive, persist to later times (400 to 450 ns, after the most characteristic $^5TT_0$ signatures have disappeared), and are likely associated with T+T. State relaxation for strongly coupled and well-aligned dimers is expected to populate $^5TT_{\pm M}$ sublevels symmetrically, e.g., a population of $^5TT_{+2}$ should result in an equal population of $^5TT_{-2}$ (6). However, preferential populations of the lower M sublevels have been observed previously (27–29).

A single crystal of TES TIPS-TT was mounted to make the orientation $z \parallel B_0$ attainable within the EPR spectrometer. Starting with $z \parallel B_0$ (labeled 0°), the sample was rotated to collect TR-EPR spectra for different orientations about the y axis in 10° increments between 0 and 180° (Fig. 5 and *SI Appendix*, Figs. S11–S13). The two center lines in Fig. 5A correspond to ^5TT transitions for strongly coupled dimers (i.e.,
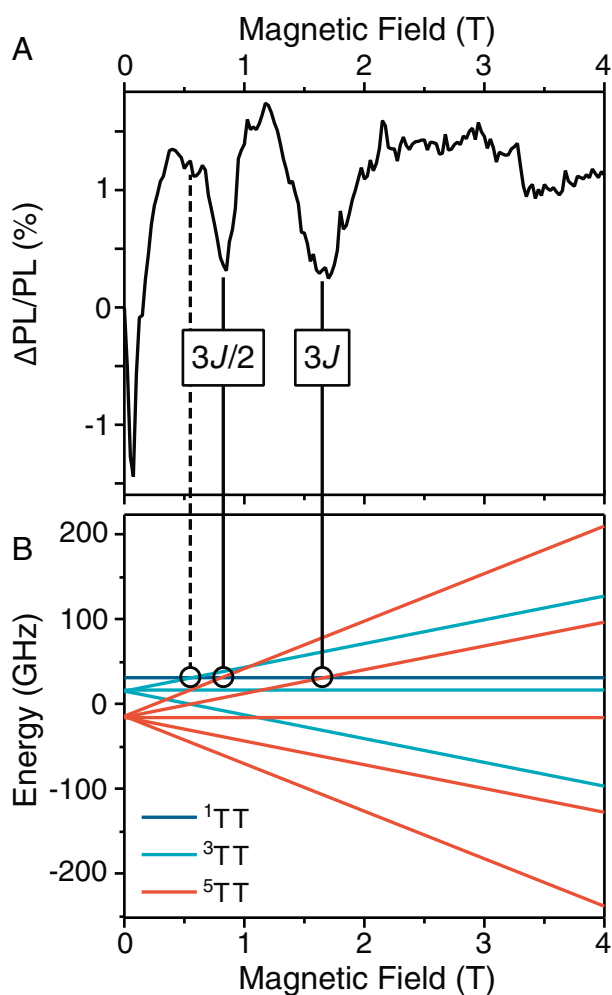

Fig. 4. Magnetophotoluminescence of TES TIPS-TT. (*A*) Changes in relative PL vs. applied magnetic field at 2 K. (*B*) Energy level diagram of an exciton pair with $J = -15.4$ GHz in a magnetic field. Black circles highlight level crossings between ^1TT and $^5TT_{+1,+2}$ (observed) and with $^3TT_{+1}$ (not observed).
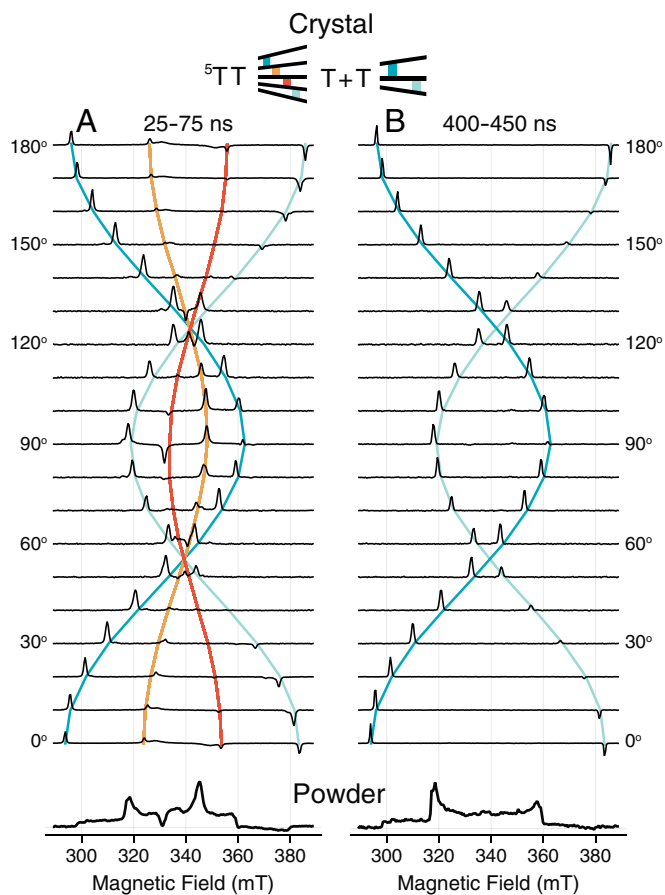
Fig. 5. TR-EPR spectra of a single crystal of TES TIPS-TT mounted to enable rotation of the molecular x and z axes in the plane of B_0 at (*A*) early (25 to 75 ns) and (*B*) late (400 to 450 ns) times. The starting orientation of 0° represents the orientation in which $z \parallel B_0$. Transitions within ^{5}TT and T+T are color-coded with identical colors being used for transitions of the same energy. Powder spectra obtained at the respective time ranges are shown at the *Bottom*.

$M = 0 \leftrightarrow M = \pm 1$), while the outer lines correspond to the degenerate set of transitions from the strongly coupled dimer ($M = \pm 1 \leftrightarrow M = \pm 2$) and uncoupled triplet ($M = 0 \leftrightarrow M = \pm 1$). Values of $D = 1{,}258$ and $E = -14$ MHz, obtained from fitting $z \parallel B_0$ and $x \parallel B_0$, were used to calculate the transitions. The values of D and E differ only slightly from the ZFS parameters extracted from the monomer triplet spectrum.

As with the crystalline powder spectra, the features associated with ^{5}TT can be roughly distinguished from those of T+T if they are detected at early times (Fig. 5*A*) but not at late times (Fig. 5*B*). Near $z \parallel B_0$ and $x \parallel B_0$, the two transitions from ^{5}TT$_0$ are easily observable as pairs of absorptive/emissive inner peaks. Intermediate orientations (e.g., 50° and 120°) have a large degree of expected overlap between transitions, but it seems that the ^{5}TT peaks are generally less prominent. The spectra at later times (Fig. 5*B*) are far simpler and feature no more than two peaks, which align well with the calculated transitions for T+T. These observations confirm the highly oriented nature of the single crystal.

The 25- to 75-ns spectra and the initial populations of the ^{5}TT and T+T sublevels were calculated at all orientations with the parallel *JDE* model as described in *Materials and Methods*. This procedure simulates the spectra at $z \parallel B_0$ (ignoring broad inner peaks) and $x \parallel B_0$ with an exceptional degree of accuracy (6). Simulations of the spectra at intermediate orientations were also successful (*SI Appendix*, Figs. S11–S13), especially regarding the predicted population of T+T. As with the

crystalline powder spectra, many spectra exhibit a trend toward preferential population of the lower energy M sublevels. Minor discrepancies between the simulation and data are evident both in peak position and amplitude and are likely related to the simplicity of the model—the spectra were simulated with only two adjustable parameters.

The change in ^{5}TT and T+T spectral amplitudes vs. delay time can be most clearly discerned at $z \parallel B_0$ (Fig. 6*A*), where ^{1}TT only relaxes into ^{5}TT$_0$, and there is no overlap between the transitions from this species and T+T. Kinetic fitting at $\theta = 0°$ (Fig. 7 and Table 2) proceeded with a 20-ns resonator response function and an exponential rise and decay, with an extended (>10 μs) decay applied to account for a small (< 5%) population of long-lived T+T. The sharp peak associated with ^{5}TT$_0 \rightarrow ^5$TT$_{+1}$ rises with $\tau = 28$ ns, whereas the $|0\rangle \rightarrow |+\rangle$ peak associated with T+T appears with $\tau = 77$ ns. However, close examination of the $|0\rangle \rightarrow |+\rangle$ kinetics reveals that the fit does not capture a portion of early signal amplitude. In line with this observation, no spectral traces were obtained (even within the resonator response time) in which ^{5}TT was observed without T+T. The same fitting procedure was also applied to $\theta = 50$ and $90°$ (*SI Appendix*, Fig. S14). TR-EPR spectra exhibit a significant degree of overlap at intermediate orientations (Fig. 5), but field points could be found that lead to sliced kinetics with negligible population after 0.5 μs (considered predominantly ^{5}TT). A comparison of the ^{5}TT kinetics at different orientations (Table 2) reveals the trend that ^{5}TT peaks persist longest at $x \parallel B_0$ and second longest at $z \parallel B_0$ and decay noticeably faster at intermediate orientations.

Discussion

Magnetic Field Effects. The observation of only two dips in emission intensity vs. magnetic field (Fig. 4) in TES TIPS-TT provides further evidence of favorable molecular alignment, unlike lower symmetry TIPS tetracene samples (*SI Appendix*, Fig. S9) (19, 20). The presence of the third dip for TIPS tetracene at magnetic fields associated with ^{1}TT/^{3}TT mixing could result from the lack of inversion center between molecular pairs and weak spin–orbit interactions. Antisymmetric spin–spin interactions (30, 31), whose magnitude may be estimated by $(\Delta g/g) J$, where g is the triplet g-factor and $\Delta g = g - g_e$, could drive such mixing. Several relevant TES TIPS-TT dimers possess inversion symmetry (Fig. 2), negating this effect, while others (e.g., dimer IA) possess a J much smaller than that of TIPS-tetracene that likely renders antisymmetric spin–spin interactions negligible.

The additional prominent feature that occurs at $B_0 < 0.1$ T in both TES TIPS-TT and TIPS tetracene is ubiquitous in early magnetic-field dependent experiments (32) on crystalline acenes. For triplet pairs with $J = 0$, states with the "singlet character" mix at fields strengths similar to the ZFS interaction. Its presence here alongside features associated with $|J| = 15.4$ GHz affirms that both paired ($|J| \gg |D|$) and unpaired ($J = 0$) triplets exist in the crystal. The potential for fast TT dissociation, inevitable in solids without well-isolated dimer-like structures, rationalizes the detection of both species in time-integrated experiments.

We note that the multitude of possible molecular pairs will lead to other values of $|J|$; however, these may not be observable in the magnetophotoluminescence experiment for various reasons, as follows: triplet–triplet interactions on these pairs may not lead to detectable fluorescence that reflects the ^{1}TT
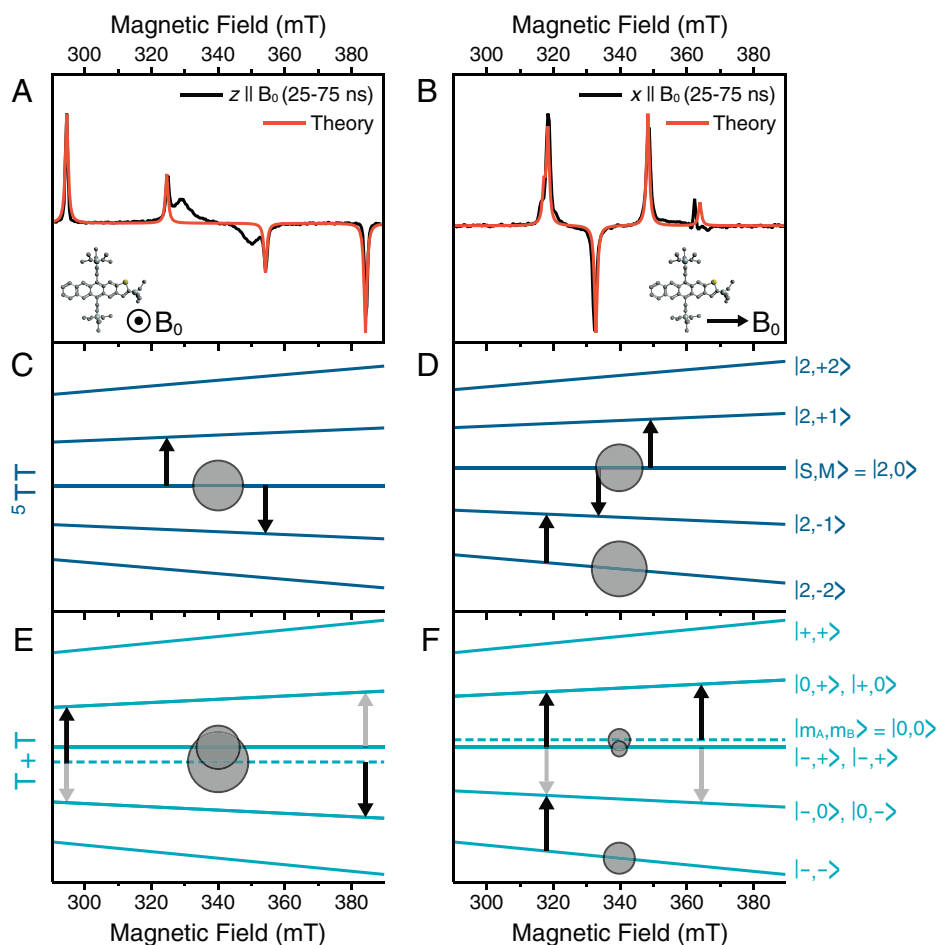
Fig. 6. Early time (25 to 75 ns) spectra and calculations of single crystal sample. Spectra are shown for (*A*) z ∥ B0 and (*B*) x ∥ B0 with associated energy level plots for (*C* and *D*) ^{5}TT and (*E* and *F*) dissociated triplets T+T. Based on the theory, the arrows indicate the field position of relevant transitions, with the associated circle areas indicating relative populations of the relevant sublevel.

population or they may be too weak or too strong to be detectable in the magnetic field range of the experiment. DFT calculations indicate $J = -15$ GHz for dimer IA, making it the site most likely responsible for the observed resonant changes in PL. Based on the calculated value for dimer II ($J = -315$ GHz), dips would be expected at 16.9 and 33.8 T, well outside the range of the current experiment. However, signals for dimer IB (DFT calc. $J = 35$ GHz) would be expected at 1.9 and 3.8 T but are not observed.

Model Rationale and Limitations. The highly successful fits of sharp TR-EPR features at all TES TIPS-TT crystal orientations underscore the successful convergence of parallel intermolecular orientation, macroscopic crystal alignment, and rigorous theory (6). A critical result of the NTT presented in this work and in ref. 6 is that the populations of the *M*-spin sublevels depend on the orientation of the chromophore pair relative to the magnetic field. The orientational dependence for sublevel populations is a prediction that is distinct from other treatments in the literature. Fig. 6 shows that the populations in the ^{5}TT$_M$ sublevels do indeed depend on orientation. But we also show that the populations of the T+T levels also depend on orientation—the quantum coherence imprinted on the singlet ^{1}TT state from SF leads to distinct, and measurable, polarizations in both the TT and the unpaired T+T spectra. Because the unpaired singlet state ^{1}TT → T+T does not have an EPR spectrum (coefficients of

$|00\rangle$, $|+-\rangle$ and $|-+\rangle$ components of ^{1}TT are equal), the assignments in Fig. 6 show that the T+T spectrum is from an unpaired quintet, as follows: ^{1}TT → ^{5}TT → T+T.

For fitting TR-EPR data, which measures population differences, the nature of the intermediate states—pure or mixed—may not be of much interest, but in prospective quantum applications involving SF, it is crucial. The singlet character approximation in the Merrifield's theory for triplet–triplet annihilation and oft-resurrected in recent literature (10, 11, 17, 22) resembles a Franck–Condon approximation, but it is unclear why such an approximation should be valid for the triplet-pair EPR spectra from SF. Therein, the putative unpaired T+T state is not a pure quantum state but rather a mixed state with a density matrix—not a wavefunction. The literature concerning the formation of this state is somewhat murky, sometimes invoking states like (T … T) that may or may not be pure quantum states. These distinctions render the *JDE* model more appropriate than Merrifield's theory for modeling the populations of TT and T+T states from SF. Further, unlike the Merrifield theory, the JDE model does consider the potentially dominant *J* interaction between chromophores that is essential for modeling the strong-field magnetophotoluminescence from curve crossings.

The simple view of the dynamics we employ, which evolves the ^{5}TT populations instantaneously, cannot be expected to be valid on all timescales. But the results we show here indicate that it is sufficient to capture many important features in the
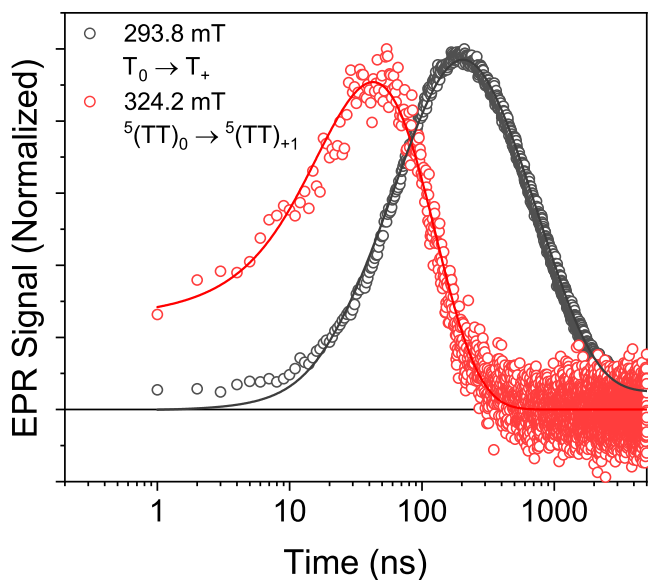
Fig. 7. Normalized kinetics at field positions where the $^5TT_0 \to {}^5TT_{+1}$ (red) and free triplet $T_0 \to T_+$ (dark gray) transitions are expected to occur at $z \parallel B_0$ ($\theta = 0°$).

observed TR-EPR spectra, and it provides microscopic insight into the unpairing process with a minimal number of empirical parameters. Below, we discuss aspects of the TES TIPS-TT TR-EPR spectra that fall outside the scope of the *JDE* model and speculate on their fundamental origins.

Spin Sublevel Populations. An explanation for the absence of the $^5TT_{+M}$ population is provided by the value $|J| = 15.4$ GHz from Fig. 4A, which leads to a crossing between the ^5TT and ^3TT manifolds, provided $J < 0$, within the magnetic field range probed by the X-band EPR experiment (300 to 400 mT, Fig. 4B and *SI Appendix*, Fig. S15). Based on experimental results obtained by Chen et al. (17), the $^5TT_{+2}/{}^3TT_{-1}$ level crossing dictated by ferromagnetic $J = -15.4$ GHz may allow for the transfer of the $^5TT_{+2}$ population to $^3TT_{-1}$. We posit that the formally forbidden interaction of these states becomes allowed due to minor deviations (static or dynamic) from pure parallel symmetry for the TES TIPS-TT dimers in the crystal, which would enable $^5TT/{}^3TT$ population transfer (but we emphasize not $^1TT/{}^3TT$ mixing without additional perturbations) (33). If TT hops between different sites during the early times of the TR-EPR experiment, a large portion of triplet pairs will at some point reside on the $J = -15.4$ GHz site within the instrument response time, allowing $^5TT_{+2} \to {}^3TT_{-1}$ transfer to occur specifically at this site. Chen et al. (17) proposed that the ^3TT manifold enables fast, spin-allowed annihilation of one of the triplets, as follows: $^3TT \to {}^3(T + S_0)$. Their mechanism would

Table 2. Time constants of the rise and decay of representative peaks of ^5TT and T+T at select orientations using a single exponential rise and decay model

Orientation	$\tau_{rise}(^5TT)$* (ns)	$\tau_{decay}(^5TT)$* (ns)	$\tau_{decay}(T + T)^\dagger$ (ns)
0° ($z \parallel B_0$)	28 ± 2 ns	86 ± 3 ns	735 ± 2 ns
50°	14 ± 5 ns	68 ± 6 ns	1211 ± 5 ns
90° ($x \parallel B_0$)	16 ± 1 ns	100 ± 1 ns	990 ± 3 ns

*At B_0 = 324, 318, 340 mT for 0, 50, 90°, respectively.
$\dagger$ At B_0 = 294, 348, 333 mT for 0, 50, 90°, respectively.

suggest that $^5TT_{+2} \to {}^3TT_{-1}$ transfer is the first step in an irreversible process that gradually filters out all exciton pairs from the $^5TT_{+2}$ state, which would be reflected in the EPR spectra even if not all TTs are occupying the $J = -15$ GHz site at the time of spin-state measurement.

The precise field position of the crossing will depend on the orientation, but as J fluctuations at specific sites are believed to follow large normal distributions at room temperature (34), a high likelihood of transient $^5TT_{+2}/{}^3TT_{-1}$ level crossings can reasonably be assumed at all field points and orientations probed here. Larger J fluctuations would be required to explain the depletion of $^5(TT)_{+1}$, and this brings forth the question about how exclusive the applied field-induced level crossing mechanism might be. We note the abundance of primarily absorptive TR-EPR spectra reported for different molecular systems (27–29) that may point toward the existence of a more general mechanism leading to an inhibited population of $^5TT_{+1,+2}$, such as the one outlined by Nagashima et al. (29) for TIPS-pentacene solids. A theoretical approach to the problem of asymmetric population transfer for a TES TIPS-TT crystal requires further investigation, but it seems likely that the direct influence of the $|J| = 15.4$-GHz site is a crucial piece of the puzzle.

Shifting and Line Broadening of TR-EPR Transitions. The broad features in the $z \parallel B_0$ spectra are much better described by a Lorentzian than a Gaussian lineshape (Fig. 8 and *SI Appendix*, Fig. S17), indicating lifetime broadening vs. inhomogeneous broadening that might otherwise dominate a long-lived species in a molecular solid (35, 36). The presence of two sets of $^5TT_0$ peaks is therefore attributed to a difference in average TT encounter times at distinct dimers, with TT at some sites being so short lived that their linewidths are dictated by lifetime broadening. The simplest analysis assuming a pure Lorentzian lineshape suggests a lifetime of roughly 0.9 ns for the broad inner peaks vs. ≥5 ns for the sharp outer peaks.

Although the proposed effect resembles the familiar exchange broadening in EPR (37), wherein spins exchange quickly between two magnetically distinct sites, its relationship to triplet pairs is tenuous. Here, the interconversion of $^5TT \leftrightarrows T+T$ reflects a fundamental change from $S = 2$ to $S = 1$ rather than the commonly analyzed case of a spin species (e.g., a hydrogen nuclei or radicals) merely undergoing a change in environment. However, our observations of broadening are consistent with TR-EPR measurements for which frequencies of interactions are comparable to the timescale of the experiment (38). The details of this apparently unique form of broadening are worthy of further investigation.

The interchromophore anisotropic interaction X, which only affects TT and is dependent on intermolecular distance and orientation, was not included in the simulations presented thus far. In the absence of X, and in the Zeeman basis, transitions involving $^5TT_{\pm 2}$ overlap perfectly with those of T+T. Consequently, contributions from X may explain the presence of small, relatively sharp side peaks neighboring T+T transitions at early times, as observed in the spectra at certain orientations (e.g., Fig. 5A at 20°). The likelihood is small that X may also be directly responsible for the broad but prominent peaks at $z \parallel B_0$ that overlap sharp transitions from $^5TT_0$. An experimental determination of the magnitude of X, currently unavailable for TES TIPS-TT, would help to uncover its role in the TR-EPR spectra.

Exciton Pair Dynamics. The higher J calculated for dimer II can largely be attributed to the closer intermolecular distance

(7), which places it in a favored position for fast triplet pair formation (39). However, this initial population imbalance at the highest J site must quickly evolve in order to explain the absorptive character of the TR-EPR spectra tentatively caused by $^5TT/^3TT$ crossing at the $J = -15$-GHz sites (dimer IA), observable even in the first 20 ns. This necessary early evolution supports the notion that, while the ^5TT signal is observed for $\tau \approx 100$ ns, TT remains at a specific site for no more than several nanoseconds, and therefore, the TR-EPR spectra reflect a shifting equilibrium of TT and dissociated T+T, residing on multiple dimer types. Although the inequality in calculated J suggests that dimers IA and IB may behave differently, we do not distinguish between them for the duration of this discussion, as the geometries are nearly identical and the calculated $J = 35$ GHz for dimer IB suggests no impact on the TR-EPR spectra via additional level crossings (*SI Appendix*, Fig. S16).

For a molecular crystal with extended order, there are multiple processes that would affect the lifetime of a particular TT species, e.g., triplet–triplet fusion or TT migration as observed in single crystals of tetracene (40). However, among these processes, the dissociation into T+T involving proximal chromophores has been studied most extensively and likely provides justification for why different TT pair lifetimes, inferred from line broadening, are found within TES TIPS-TT. Triplet-pair
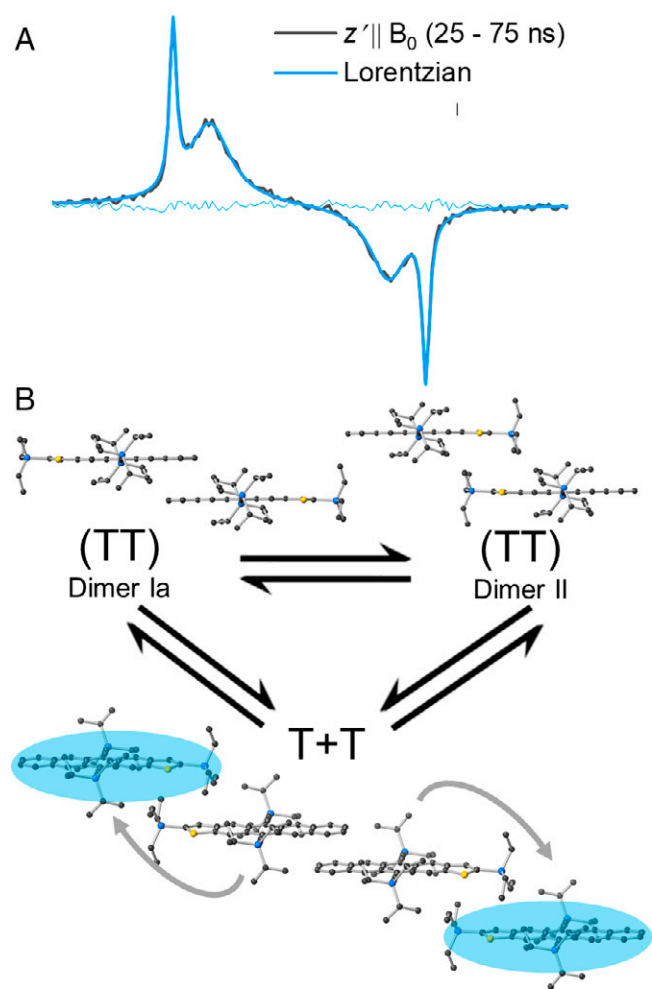

Fig. 8. Dynamic picture of triplet-pair populations. (*A*) Early time TR-EPR spectrum and fit to Lorentzian lineshape, characteristic of two types of lifetime-broadened quintets. (*B*) Depiction of equilibrium between distinct TT sites and dissociated T+T, also highlighted within the TES TIPS-TT crystal structure. Gray arrows and blue ovals indicate one possible route toward (T+T) formation from dimer II (TT).

dissociation has often been modeled using the so-called "transfer integral" approach (41), which estimates coupling energies that facilitate the hopping of one member of TT to a neighboring chromophore. Single-exciton hopping rate constants for specific systems, such as TIPS pentacene, are derived from optical measurements involving bimolecular decay (42–44), revealing that varying electronic coupling can lead to subnanosecond hopping or make it prohibitively slow compared to unimolecular triplet decay (27).

When dimer IA is considered, the relevant pair for the transfer integral is dimer II because the outlet for triplet pair dissociation involves the proximal molecules that form the phenyl-overlapped, vs. the thiophene-overlapped, geometry (Fig. 8*B*). As has been shown theoretically (45), slippage both along and perpendicular to the molecular long axis results in a modulation of both J and the transfer integral that can lead to displaced maxima for these quantities. As such, the transfer integral for TT dissociation at dimer IA could be relatively small, leading to a persistence of the exchange-coupled triplet pair at that site. Conversely, fast dissociation of the triplet pair at dimer II could be facilitated by a large transfer integral associated with thiophene-overlapped molecules (geometry of dimer IA/b), and the broad inner quintet peaks are reflective of their fleeting population. A reliable transfer integral calculation is beyond the scope of this manuscript, but we note that with average triplet diffusion coefficients around 10^{-3} cm^2/s (46), hopping along the c axis (unit cell parameter ~ 21 Å), which is approximately parallel to the π-stacked staircase, would occur with a rate constant of roughly 2×10^8 s^{-1}. Further, the short-axis slippage of dimer II could lead to a slower rate constant of triplet motion that keeps the triplet pair at dimer IA intact for longer than triplet pairs at dimer II.

Given that ^5TT and T+T are present from the earliest TR-EPR observation times, we propose that the <100-ns delay signals are representative of the equilibrium $^5TT \rightleftharpoons$ T+T, with the narrow and broad ^5TT peaks associated with the $J = -15$ GHz and $J = -315$ GHz sites, respectively. The disappearance of ^5TT features is associated with a loss of spin coherence and decrease in exciton density due to population decay and eventual hopping orthogonal to the fastest transport direction, leading to fewer opportunities to refuse and generate ^5TT. The different decay rates of the ^5TT peaks (Table 2) suggest that the equilibrium decay may also be faster at intermediate orientations (47, 48). We also note that the degree of broadening exhibits some orientation dependence (Fig. 6, compare the $^5TT_0$ transition peaks in $z \parallel B_0$ to $x \parallel B_0$). This may be caused by effects related to anisotropic hopping rates of triplets along different crystal directions or orientation-dependent spin-state interconversion (44, 49). Although we have not directly measured exciton transport for TES TIPS-TT, in rubrene, a transition from one-dimensional to multidimensional triplet diffusion occurs on the 100s of nanoseconds timescale (50), similar to ^5TT decay times observed here and implying a transport-related mechanism of triplet-pair population loss.

Conclusions. We have presented a comprehensive analysis of the spin dynamics of triplet pairs in the organic compound TES TIPS-TT, which forms crystals that enforce parallel molecular alignment not yet tested in studies of triplet-pair spin polarization. By comparing TR-EPR spectra at various orientations with respect to the applied magnetic field with calculations using the *JDE* model, we conclude that 1) with B_0 parallel to the z magnetic axis of the molecules, $^5TT_0$ is exclusively formed from ^1TT, with T+T emerging nearly simultaneously through the $^5TT_0$ parent; 2) anomalous T_{-1} is observed through funneling of population

near a level crossing predicted by exchange coupling measurements; 4) distinct ^{5}TT populations form in separate pairs that undergo nanosecond-scale dissociation. The results validate the proposed *JDE* model for strongly and weakly exchanged coupled pairs while suggesting that dynamics associated with interactions beyond the dimer in which TT was first formed introduce unpredicted behaviors. The question remains if these behaviors can be advantageous in certain QI applications or if they can be reduced with an additional level of crystal engineering that further isolates dimers while maintaining strict alignment. Control of spin sublevel population in this fashion advances toward the goal of harnessing triplet pairs as optically driven elements of QI processing.

Materials and Methods

Experimental Details.

Structural characterization. X-ray diffraction data were collected at 90.0(2) K on a Bruker D8 Venture dual-source diffractometer with graded-multilayer focused MoK(alpha) X-rays. Raw data were integrated, scaled, merged, and corrected for Lorentz-polarization effects using the APEX3 package. Corrections for absorption were applied using the SADABS program (51). The structures were solved by dual-space methods (SHELXT) (52) and refined against F^2 by weighted full-matrix least-squares (SHELXL-2018) (53). Hydrogen atoms were found in difference maps but subsequently placed at calculated positions and refined using riding models. Nonhydrogen atoms were refined with anisotropic displacement parameters. The final structure model was checked using established methods (54, 55). Atomic scattering factors were taken from the International Tables for Crystallography (56). Additional crystal data and information on structure refinement can be found in *SI Appendix*.

Magnetophotoluminescence. Column-shaped TES TIPS-TT crystals were attached to glass substrates using silver adhesive and then positioned at the face of a 50-μm-diameter multimode optical fiber. The fiber was one port of a 50:50 coupler linking the sample with the excitation and detection arms. The excitation source was a filtered 519-nm diode laser operated below threshold giving an unpolarized power of 1 μW exiting the sample arm. Photoluminescence (PL) collected there reached the detection arm where it was coupled through a 539-nm edge filter and into a 0.27-m spectrometer with a cooled charged-coupled device array. The sample arm was held in He vapor within a 2 K, 0-14 T magnet (Quantum Designs, Dynacool) with the field oriented perpendicular to the long axis of the crystal.

EPR spectroscopy. TR-EPR experiments at X-band ($\approx$9.5 GHz) were performed using a Bruker Elexsys E-580 spectrometer equipped with an ER 4118X-MS3 resonator. Spectra were collected after photoexcitation with 7-ns, $\approx$2.5-mJ pulses from an Opotek Radiant 355 LD laser system under constant irradiation with a microwave power of 2.4 mW. The quality factor of the resonator was measured to be between 500 and 700 for experiments on single crystal samples for which the kinetics were analyzed, indicating an expected resonator response function between 16 and 23 ns. Based on the average of these values, a resonator response of 20 ns was used for kinetic fitting.

The TIPS TES-TT monomer triplet spectrum was collected from a sample consisting of the material dissolved in a 4:1 mixture of iodobutane and toluene prepared in the glovebox, temporarily sealed with a septum, frozen using liquid N₂, and then rapidly transferred to the EPR spectrometer held at 100 K to prevent oxygen from dissolving into the solvent matrix of the sample. The crystalline powder sample was prepared by placing glass capillaries coated with small amounts of crystalline powder into clear fused quartz (CFQ) EPR tubes, which were then flame sealed under vacuum. Four single crystal samples were mounted using the (0 1 -1) or (0 -1 1) faces to the end of CFQ rods cut at 38° in a manner shown in photos provided in *SI Appendix*. Using a goniometer manufactured by Bruker, multiple spectra were taken for each sample to determine the orientation (within 2°) at which the splitting between the two peaks assigned to diffuse triplets was the largest. As the largest splitting between triplet transitions is expected to occur when the primary molecular z axis is parallel to the applied magnetic field, the sample exhibiting the largest splitting was chosen as the most well-aligned and was used for further analysis.

Theoretical Development and Calculations.

Theoretical development. To model the exciton unbinding process, we let the *J*-coupling be binary–it is *J* when two molecules in the crystal are nearest neighbors and zero otherwise. The Hamiltonian takes the form,

$$\mathcal{H} = H_{Zeeman,AB} + H_{ZFS,A} + H_{ZFS,B} + f(J\vec{S}_A \cdot \vec{S}_B), \qquad [1]$$

for chromophores *A* and *B* where *f* is a binary switching function that is either zero or one. While the ^{1}TT state forms on adjacent chromophores (8), the excitons in a crystal are mobile. Once one of the excitons hops to another chromophore, the ^{1}TT state can decohere and evolve to separated triplet pairs, T+T.

Part of the spectrum comes from the ^{5}TT$_M$ sublevels, whose calculations appear in the analysis of the parallel *JDE* model in an earlier publication (6). But in a crystal, some of the triplets in the ensemble will have hopped and unpaired, even at early times. We assume that the jump dynamics are slow relative to the timescale for quintet formation on neighboring molecules but fast enough to completely dephase the triplet pair states. We model this by allowing the quintet state to form for all molecules in the *JDE* Hamiltonian, $f = 1$. Some fraction of those molecules in the ensemble will experience a jump between time 0 and time t. That subensemble will quench into the unpaired triplet Hamiltonian, $f = 0$. We quench those molecules, using the density matrix from the initial quintet states of the *JDE* model, into the states of the unpaired triplet by applying the projection operator $P = \sum_{M_A, M_B} |M_A, M_B\rangle\langle M_A, M_B|$, where the sum over M_A and M_B goes over the sublevels of unpaired states–the eigenstates of the Hamiltonian with $f = 0$. The projection operator separates the diagonal elements of the density matrix in the unpaired basis. The density matrix of the entire system is $\rho = w\rho_0 + (1 - w)P\rho_0 P$, where w is an empirical parameter equivalent to the fraction of exciton pairs that have not undergone a jump before the time of measurement, and ρ_0 is the density matrix of the *JDE* model at early times (6). Here, we are assuming that the populations decouple from the coherences and that the time evolution of the coherences is fast compared to the populations. Both approximations appear in the Redfield theory of quantum relaxation (57). The calculation of the TR-EPR spectrum follows from the density matrix (6).

TES TIPS-TT TR-EPR calculations. The single crystal spectra of TES TIPS-TT at select orientations were calculated with the parallel *JDE* model, where both transitions and intensities are calculated from the spin Hamiltonian (Eq. **1**). The computed TR-EPR spectra at each orientation are sums of two components, as follows: one from the ^{5}TT$_M$ sublevels and another from the spin-polarized, unpaired triplets T+T. First, the calculated spectrum was compared to the data for $z \parallel B_0$ to optimize a value of D in the least-squares sense with the simulated annealing technique. At this orientation, E has little to no effect on the spectrum. Fixing D to the resulting best-fit value (1,260 MHz), the $x \parallel B_0$ spectrum was optimized for E (-16 MHz). When optimizing parameters, the Hamiltonian is evaluated in the eigenbasis of the quintet subspace, which we call the adiabatic basis,

$$\left| S = 2, \alpha \right\rangle = \sum_M \alpha_M \left| S = 2, M \right\rangle.$$ These states are very close to the Zeeman $| S = 2, M\rangle$ states away from crossings (33). Although the energies of the Zeeman states change upon sample rotation, the states remain well defined. The ^{5}TT and T+T populations were calculated using the parallel *JDE* model (see above), but to replicate the data, populations of the two high energy quintet states ($M = +1, +2$) were set to zero. The four ^{5}TT and two T+T lines ($\Delta M = \pm 1$) at each orientation are broadened by Lorentzian lineshapes. Line intensities are proportional to the difference in population between the $\Delta M = \pm 1$ sublevels and the corresponding dipole matrix element squared. The relative amplitudes of the ^{5}TT and T+T spectra are orientation dependent and are estimated from the data. Diagrams of the spin sublevel energies and populations (Fig. 5 *C–F* and *SI Appendix*, Figs. S11–S13) were likewise calculated but in the diabatic Zeeman basis where states of S and M are long-lived.

Monomer ^{3*}(TES TIPS-TT) TR-EPR calculations. The monomer ^{3*}(TES TIPS-TT) powder EPR spectrum was calculated by evaluating the spin Hamiltonian $\mathcal{H} = H_{Zeeman} + H_{ZFS}$ in the single triplet exciton (T) eigenbasis. The simulated annealing optimization method found the best-fit parameters D = 1,273 MHz and E = -40 MHz. ISC populates the zero-field triplet states $|x\rangle$, $|y\rangle$, and $|z\rangle$. Because the NTT in the *JDE* model is for triplet pairs, the zero-field populations are fit parameters ($p_x = 0.11$, $p_y = 0.11$, and $p_z = 0.78$). To simulate the powder EPR spectrum, Hamiltonians were calculated for a spherical distribution of orientations describing the relative orientation of the chromophore with respect

Author affiliations: [a]Chemistry and Nanosciences Center, National Renewable Energy Laboratory, Golden, CO 80401; [b]Department of Chemistry, University of Colorado Boulder, Boulder, CO 80309; [c]Renewable and Sustainable Energy Institute, University of Colorado Boulder, Boulder, CO 80309; [d]Center for Applied Energy Research, University of Kentucky, Lexington, KY 40511; and [e]Department of Chemistry, University of Kentucky, Lexington, KY 40506

1. D. P. DiVincenzo, The physical implementation of quantum computation. *Fortschr. Phys.* **48**, 771–783 (2000).
2. N. P. d. Leon *et al.*, Materials challenges and opportunities for quantum computing hardware. *Science* **372**, eabb2823 (2021).
3. M. R. Wasielewski *et al.*, Exploiting chemistry and molecular systems for quantum information science. *Nat. Rev. Chem.* **4**, 490–504 (2020).
4. A. Gaita-Ariño, F. Luis, S. Hill, E. Coronado, Molecular spins for quantum computation. *Nat. Chem.* **11**, 301–309 (2019).
5. C. J. Bardeen, Time dependent correlations of entangled states with nondegenerate branches and possible experimental realization using singlet fission. *J. Chem. Phys.* **151**, 124503 (2019).
6. K. E. Smyser, J. D. Eaves, Singlet fission for quantum information and quantum computing: The parallel JDE model. *Sci. Rep.* **10**, 18480 (2020).
7. G. D. Scholes, Correlated pair states formed by singlet fission and exciton–exciton annihilation. *J. Phys. Chem. A* **119**, 12699–12705 (2015).
8. P. E. Teichen, J. D. Eaves, Collective aspects of singlet fission in molecular crystals. *J. Chem. Phys.* **143**, 044118 (2015).
9. S. L. Bayliss *et al.*, Probing the wave function and dynamics of the quintet multiexciton state with coherent control in a singlet fission material. *Phys. Rev. X* **10**, 021070 (2020).
10. L. R. Weiss *et al.*, Strongly exchange-coupled triplet pairs in an organic semiconductor. *Nat. Phys.* **13**, 176–181 (2017).
11. R. M. Jacobberger, Y. Qiu, M. L. Williams, M. D. Krzyaniak, M. R. Wasielewski, Using molecular design to enhance the coherence time of quintet multiexcitons generated by singlet fission in single crystals. *J. Am. Chem. Soc.* **144**, 2276–2283 (2022).
12. J. J. L. Morton *et al.*, Solid-state quantum memory using the 31p nuclear spin. *Nature* **455**, 1085–1088 (2008).
13. M. S. Fataftah, D. E. Freedman, Progress towards creating optically addressable molecular qubits. *Chem. Commun. (Camb.)* **54**, 13773–13781 (2018).
14. M. S. Fataftah *et al.*, Trigonal bipyramidal v3+ complex as an optically addressable molecular qubit candidate. *J. Am. Chem. Soc.* **142**, 20400–20408 (2020).
15. S. L. Bayliss *et al.*, Optically addressable molecular spins for quantum information processing. *Science* **370**, 1309–1312 (2020).
16. M. B. Smith, J. Michl, Singlet fission. *Chem. Rev.* **110**, 6891–6936 (2010).
17. M. Chen *et al.*, Quintet-triplet mixing determines the fate of the multiexciton state produced by singlet fission in a terrylenediimide dimer at room temperature. *Proc. Natl. Acad. Sci. U.S.A.* **116**, 8178–8183 (2019).
18. M. I. Collins, D. R. McCamey, M. J. Y. Tayebjee, Fluctuating exchange interactions enable quintet multiexciton formation in singlet fission. *J. Chem. Phys.* **151**, 164104 (2019).
19. S. L. Bayliss *et al.*, Site-selective measurement of coupled spin pairs in an organic semiconductor. *Proc. Natl. Acad. Sci. U.S.A.* **115**, 5077–5082 (2018).
20. S. L. Bayliss *et al.*, Spin signatures of exchange-coupled triplet pairs formed by singlet fission. *Phys. Rev. B* **94**, 045204 (2016).
21. D. Lubert-Perquel *et al.*, Identifying triplet pathways in dilute pentacene films. *Nat. Commun.* **9**, 4222 (2018).
22. M. J. Y. Tayebjee *et al.*, Quintet multiexciton dynamics in singlet fission. *Nat. Phys.* **13**, 182–188 (2017).
23. Y. J. Bae *et al.*, Spin dynamics of quintet and triplet states resulting from singlet fission in oriented terrylenediimide and quaterrylenediimide films. *J. Phys. Chem. C* **124**, 9822–9833 (2020).
24. S. L. Bayliss *et al.*, Tuning spin dynamics in crystalline tetracene. *J. Phys. Chem. Lett.* **10**, 1908–1913 (2019).
25. M. L. Tang, A. D. Reichardt, T. Siegrist, S. C. B. Mannsfeld, Z. Bao, Trialkylsilylethynyl-functionalized tetraceno[2,3-b]thiophene and anthra[2,3-b]thiophene organic transistors. *Chem. Mater.* **20**, 4669–4676 (2008).
26. E. J. Taffet, D. Beljonne, G. D. Scholes, Overlap-driven splitting of triplet pairs in singlet fission. *J. Am. Chem. Soc.* **142**, 20040–20047 (2020).
27. N. A. Pace *et al.*, Conversion between triplet pair states is controlled by molecular coupling in pentadithiophene thin films. *Chem. Sci. (Camb.)* **11**, 7226–7238 (2020).
28. I. Papadopoulos *et al.*, Varying the interpentacene electronic coupling to tune singlet fission. *J. Am. Chem. Soc.* **141**, 6191–6203 (2019).
29. H. Nagashima *et al.*, Singlet-fission-born quintet state: Sublevel selections and trapping by multiexciton thermodynamics. *J. Phys. Chem. Lett.* **9**, 5855–5861 (2018).
30. T. Moriya, Anisotropic superexchange interaction and weak ferromagnetism. *Phys. Rev.* **120**, 91 (1960).
31. T. Moriya, New mechanism of anisotropic superexchange interaction. *Phys. Rev. Lett.* **4**, 228 (1960).
32. R. E. Merrifield, Magnetic effects on triplet exciton interactions. *Pure Appl. Chem.* **27**, 481–498 (1971).
33. S. G. Lewis, K. E. Smyser, J. D. Eaves, Clock transitions guard against spin decoherence in singlet fission. *J. Chem. Phys.* **155**, 194109 (2021).
34. J. Aragó, A. Troisi, Dynamics of the excitonic coupling in organic crystals. *Phys. Rev. Lett.* **114**, 026402 (2015).
35. W.R. Hagen, Dislocation strain broadening as a source of anisotropic linewidth and asymmetrical lineshape in the electron paramagnetic resonance spectrum of metalloproteins and related systems. *J. Magn. Reson. (1969)* **44**, 447–469 (1981).
36. C. P. Poole, H. A. Farach, Line shapes in electron spin resonance. *Bull. Magn. Reson.* **1**, 162–194 (1979).
37. J. A. Weil, J. R. Bolton, *Electron Paramagnetic Resonance: Elementary Theory and Practical Applications* (John Wiley & Sons, 2007).
38. M. D. E. Forbes, L. E. Jarocha, S. Sim, V. F. Tarasov, "Time-resolved electron paramagnetic resonance spectroscopy: History, technique, and application to supramolecular and macromolecular chemistry" in *Advances in Physical Organic Chemistry*, I. H. Williams, N. H. Williams, Eds. (Academic Press, 2013), **vol. 47**, pp. 1–83.
39. J. C. Johnson, A. J. Nozik, J. Michl, The role of chromophore coupling in singlet fission. *Acc. Chem. Res.* **46**, 1290–1299 (2013).
40. Y. Wan, G. P. Wiederrecht, R. D. Schaller, J. C. Johnson, L. Huang, Transport of spin-entangled triplet excitons generated by singlet fission. *J. Phys. Chem. Lett.* **9**, 6731–6738 (2018).
41. J. Wehner, B. Baumeier, Intermolecular singlet and triplet exciton transfer integrals from many-body green's functions theory. *J. Chem. Theory Comput.* **13**, 1584–1594 (2017).
42. C. Grieco *et al.*, Triplet transfer mediates triplet pair separation during singlet fission in 6,13-bis(triisopropylsilylethynyl)-pentacene. *Adv. Funct. Mater.* **27**, 1703929 (2017).
43. G. S. Doucette *et al.*, Tuning triplet-pair separation versus relaxation using a diamond anvil cell. *Cell Rep. Phys. Sci.* **1**, 100005 (2020).
44. R. J. Hudson, D. M. Huang, T. W. Kee, Anisotropic triplet exciton diffusion in crystalline functionalized pentacene. *J. Phys. Chem. C* **124**, 23541–23550 (2020).
45. V. Abraham, N. J. Mayhall, Revealing the contest between triplet–triplet exchange and triplet–triplet energy transfer coupling in correlated triplet pair states in singlet fission. *J. Phys. Chem. Lett.* **12**, 10505–10514 (2021).
46. T. Zhu, Y. Wan, Z. Guo, J. Johnson, L. Huang, Two birds with one stone: Tailoring singlet fission for both triplet yield and exciton diffusion length. *Adv. Mater.* **28**, 7539–7547 (2016).
47. A. Schweiger, G. Jeschke, *Principles of Pulse Electron Paramagnetic Resonance* (Oxford University Press, ed. 1, 2001).
48. N. F. Berk, J. Rosenthal, L. Yarmus, Spin relaxation of triplet excitons in molecular crystals. *Phys. Rev. B* **28**, 4963–4969 (1983).
49. W. Bizzaro, J. Rosenthal, N.F. Berk, L. Yarmus, The EPR linewidth of triplet excitons in single-crystal anthracene: A re-examination. *Solid State Phys.* **84**, 27–32 (1977).
50. E. A. Wolf, I. Biaggio, Geminate exciton fusion fluorescence as a probe of triplet exciton transport after singlet fission. *Phys. Rev. B* **103**, L201201 (2021).
51. L. Krause, R. Herbst-Irmer, G. M. Sheldrick, D. Stalke, Comparison of silver and molybdenum microfocus X-ray sources for single-crystal structure determination. *J. Appl. Cryst.* **48**, 3–10 (2015).
52. G.M. Sheldrick Shelxt - integrated space-group and crystal-structure determination. *Acta Crystallogr. A* **71**, 3–8 (2015).
53. G. M. Sheldrick, Crystal structure refinement with SHELXL. *Acta Crystallogr. C Struct. Chem.* **71**, 3–8 (2015).
54. S. Parkin, Expansion of scalar validation criteria to three dimensions: The R tensor. Erratum. Erratum. *Acta Crystallogr. A* **56**, 317 (2000).
55. A. L. Spek, Structure validation in chemical crystallography. *Acta Crystallogr. D Biol. Crystallogr.* **65**, 148–155 (2009).
56. A. J. C. Wilson, *International Tables for Crystallography. Volume C: Mathematical,* Physical and Chemical Tables (Kluwer Academic Publishers, Holland, 1992).
57. K. Blum, *Density Matrix Theory and Applications* (Springer Science & Business Media, 2012).